Atomic and electronic structures of FeSe monolayer and bilayer thin films on SrTiO₃ (001): First-principles study

Kai Liu,[1] Zhong-Yi Lu,[1,*] and Tao Xiang[2,3,†]

[1]*Department of Physics, Renmin University of China, Beijing 100872, China*
[2]*Institute of Theoretical Physics, Chinese Academy of Sciences, Beijing 100190, China*
[3]*Institute of Physics, Chinese Academy of Sciences, Beijing 100190, China*

By using first-principles calculations, we have studied the atomic and electronic structures of FeSe monolayer and bilayer thin films on SrTiO₃ (001) with SrO or TiO₂ termination. We find that both FeSe monolayer and bilayer on either termination behave like a slightly doped semiconductor with a collinear antiferromagnetic order on Fe ions. FeSe is adhered to the SrTiO₃ surface by a dipole-dipole interaction. The Fermi surface is mainly of the contribution of Fe-3d orbitals. The valence band contributed mainly by the O-2p orbitals in the TiO₂ layer is located slightly below the Fermi level, which can become conducting upon a small doping of holes. For electron-doped SrTiO₃ (001) with TiO₂ termination, the Fermi level and the energy bands of the FeSe monolayer shift into the energy band gap of the substrate.

I. INTRODUCTION

The discovery of Fe-based superconductors[1–4] has inspired worldwide interests both experimentally and theoretically in the recent years. The common feature of all the Fe-based superconductor compounds is that they have FeX layers (X = P, As, S, Se, or Te) composed of edge-sharing tetrahedra with an Fe center. Furthermore, some of the parent compounds of these superconductors are antiferromagnetic (AFM) semimetals[5] with either collinear[6,7] or bicollinear[8,9] AFM order below a structural transition temperature. The superconductivity can be induced either by hole or electron doping via chemical substitution or by high pressure, and the superconducting pairing is believed to occur in the FeX layers.

In Fe-based superconductors, it was widely believed that the As-bridged antiferromagnetic superexchange interaction between the next-nearest-neighboring Fe-Fe atoms plays an important role.[7,10] This kind of interaction depends strongly on the local geometry of an Fe-As bond. Indeed, it was found that the geometry of the FeX_4 tetrahedral unit, in particular, the bond length and the bond angle between two neighboring X and Fe ions, strongly correlates with the superconductivity transition temperature.[11,12] Aside from applying pressure, growing an Fe-based superconductor on some substrate is another effective way to manipulate the lattice parameters and the FeX_4 tetrahedral geometry, which may tune the superconducting transition temperature. As an orthodox metal-oxide perovskite, strontium titanate (SrTiO₃) is widely used as a high-quality substrate for epitaxial growth of high-temperature cuprate superconductors and many other oxide-based thin films.[13] Very recently, SrTiO₃ has been used as a substrate to epitaxially grow FeSe ultrathin films.[14] It is found that the monolayer FeSe thin film grown on SrTiO₃ (001) shows signatures of superconducting transition above 50 K by transport measurement, while the bilayer and thicker films, in contrast, do not show any sign of superconductivity.[14]

To understand the physics underlying this remarkable finding, we have performed the first-principles electronic-structure calculations on FeSe monolayer and bilayer ultrathin films on SrTiO₃ (001), respectively. We find that both monolayer and bilayer thin films show a semiconducting behavior with a collinear AFM order on Fe atoms, much different from the metallic bulk FeSe. Considering the difference between the single-layer FeSe and multilayer FeSe thin films, this suggests that the observed superconductivity happens either at the interface of FeSe-SrTiO₃ or just in the first FeSe layer, not in the other FeSe layers. In the experiment reported in Ref. 14, the substrate was electron doped by introducing oxygen vacancies or Nb doping. To model this electron-doping effect, we have calculated the band structure by replacing a small portion of O atoms by F atoms using the conventional virtual-crystal approximation. We hope this can allow us to gain a qualitative picture on the effect of electron doping.

Crystal SrTiO₃ is built from alternatively stacking planar SrO and TiO₂ square layers along the c axis. Experimentally, bulk SrTiO₃ takes a structural phase transition from cubic perovskite structure into a tetragonal one at 105 K, in which each octahedral unit TiO₆ with titanium centered slightly rotates around the z axis, meanwhile the rotation directions between the nearest-neighboring octahedral units are reverse with each other.[15,16] Such a structural distortion is thus called antiferrodistortion.

The cleaving of SrTiO₃ simultaneously generates both SrO- and TiO₂-terminated surfaces with the corresponding cleavage energy equally distributed between these two surfaces.[17,18] It was further shown that the surface energies are nearly the same for these two surfaces after full relaxation.[18,19] This means that both surfaces are stable and either of them may be used as a substrate to grow FeSe thin films. We thus study the FeSe monolayer and bilayer on both TiO₂- and SrO-terminated SrTiO₃ (001), respectively.

II. COMPUTATIONAL DETAILS

To study the atomic structures and the electronic and magnetic properties of FeSe ultrathin films on SrTiO₃ (001), we carried out the fully spin-polarized first-principles electronic-structure calculations by using the projector augmented wave (PAW) method.[20,21] We adopted the

generalized gradient approximation of Perdew-Burke-Ernzerhof[22] for the exchange-correlation potentials. After the full convergence test, the kinetic energy cutoff of the plane-wave basis was chosen to be 400 eV. The optimization made the forces on all relaxed atoms smaller than 0.02 eV/Å.

We first checked the properties of bulk $SrTiO_3$. We constructed a 20-atom tetragonal supercell so that we can describe the antiferrodistortive structure, the unit cell of which is $\sqrt{2} \times \sqrt{2} \times 2$ unit cell of undistortive bulk $SrTiO_3$. The Brillouin zone was sampled with a $6 \times 6 \times 6$ **k**-point mesh. After both the shape and volume of the supercell and the internal atomic positions were optimized, we find that $SrTiO_3$ has indeed an antiferrodistortive tetragonal structure with the lattice parameters $a^\star = b^\star = \sqrt{2}a = 5.536$ Å and $c^\star = 2c = 7.831$ Å (a and c being the lattice parameters of the undistortive tetragonal unit cell), the octahedral rotation angle $\theta = 1.1°$, and the ratio $(c/a) - 1 = 3 \times 10^{-4}$. These values agree well with the experimental data[16] $a^\star = b^\star = 5.507$ Å, $c^\star = 7.796$ Å, $\theta = 2.1°$, and $(c/a) - 1 = 10 \times 10^{-4}$, respectively, as well as with the previous calculation results.[23]

To model FeSe ultrathin films on TiO_2- (SrO-) terminated $SrTiO_3$ (001), we used a six- (seven-) layer $SrTiO_3$(001) slab with the FeSe monolayer and bilayer adsorbed on the top side in a $\sqrt{2}a \times \sqrt{2}a$ two-dimensional supercell plus a vacuum layer of about 10 Å. The top two slab layers and all FeSe layer atoms were allowed to relax, while the bottom slab layers were fixed at their bulk positions. A $6 \times 6 \times 1$ **k**-point mesh for the Brillouin zone sampling and the Gaussian smearing technique with a width of 0.1 eV were used. The electric field induced by asymmetric slab relaxation was compensated by a dipole correction.[24]

III. RESULTS AND ANALYSIS

For both TiO_2- and SrO-terminated $SrTiO_3$ substrates, we studied two possible adsorption structures of FeSe thin films as shown in Figs. 1(a), 1(b), 2(a), and 2(b), respectively. The nonmagnetic, ferromagnetic, checkerboard antiferromagnetic Néel, and collinear antiferromagnetic states were all calculated. Patterns of Fe atom spins in the checkerboard antiferromagnetic Néel and the collinear antiferromagnetic states are shown in panels (c) and (d) of Figs. 1 and 2, respectively. To better understand the electronic properties of FeSe thin films on $SrTiO_3$, the electronic band structures of clean $SrTiO_3$ surface and isolated FeSe monolayer are first introduced in Sec. III A. The calculated results of monolayer and bilayer FeSe ultrathin films on TiO_2-terminated and SrO-terminated $SrTiO_3$ are then presented in Secs. III B and III C, respectively. In Sec. III D, we further introduce the electron-doping effect.

Figure 1 shows the atomic structures of monolayer FeSe on the TiO_2-terminated $SrTiO_3$ surface. For structure I in Fig. 1(a), a Se atom locates on the top of a Ti atom, which substitutes the position of an O atom in TiO_6 octahedron of bulk $SrTiO_3$. For structure II in Fig. 1(b), a Se atom sits on the center site of the Ti-Ti square. The atomic structures of monolayer FeSe on the SrO-terminated $SrTiO_3$ surface are shown in Fig. 2. For structure I in Fig. 2(a), a Se atom locates on the top of an O atom. As to the structure II in Fig. 2(b), a Se atom is on the top of a Sr atom. By considering the symmetry of both the ad-
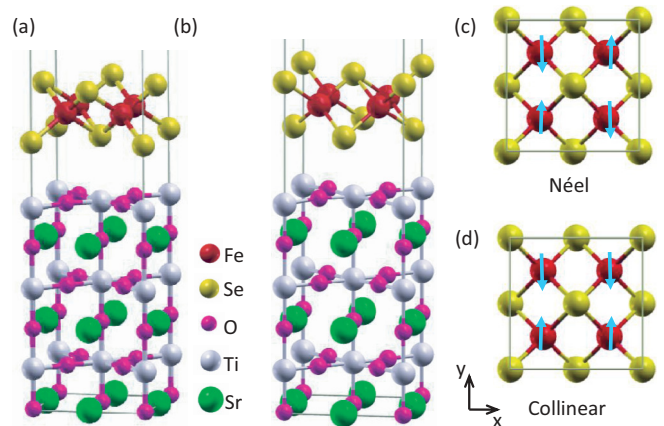
FIG. 1. (Color online) Atomic structures (a) I and (b) II of monolayer FeSe on TiO_2-terminated $SrTiO_3$(001) surface. Patterns of Fe atom spins in (c) checkerboard antiferromagnetic Néel state and (d) collinear antiferromagnetic state.

layer and the substrate, these four structures in Figs. 1 and 2 are the most possible adsorption sites.

A. Clean $SrTiO_3$ surface and isolated FeSe monolayer

In order to have a concept about how the electronic structures of FeSe-$SrTiO_3$ heterostructures are derived from their subdivisions, we first studied the band structures of TiO_2- and SrO-terminated $SrTiO_3$ (001) clean surfaces and isolated FeSe monolayer, respectively. For the SrO-terminated surface, the atomic structure of a seven-layer slab is the same as the substrate of $\sqrt{2}a \times \sqrt{2}a$ two-dimensional supercell in Fig. 2. For the TiO_2-terminated case, the TiO_2 and SrO layers exchange their vertical positions. Regarding the isolated FeSe monolayer, its in-plane lattice constants were fixed at the value of the $SrTiO_3$ surface as in Fig. 1. This corresponds to 3.91 Å for the in-plane distance of Se-Se atom. We also checked the case of 3.8 Å as reported in the experiment.[14] There is no meaningful change found.

Figure 3 shows the band structures of clean TiO_2- and SrO-terminated $SrTiO_3$ surfaces in panels (a) and (b), respectively.
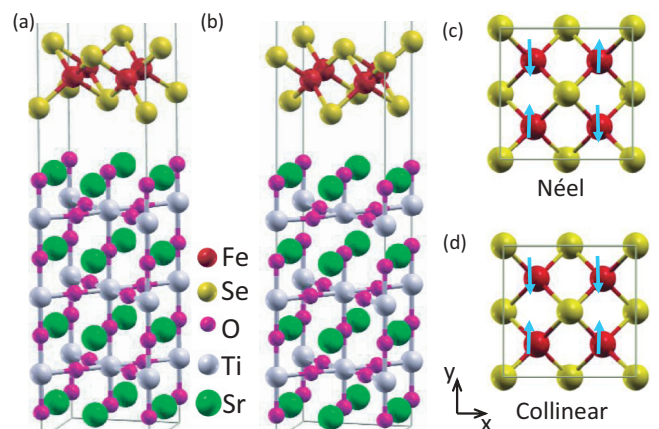
FIG. 2. (Color online) Atomic structures (a) I and (b) II of monolayer FeSe on SrO-terminated $SrTiO_3$ (001) surface. Patterns of Fe atom spins in (c) checkerboard antiferromagnetic Néel state and (d) collinear antiferromagnetic state.
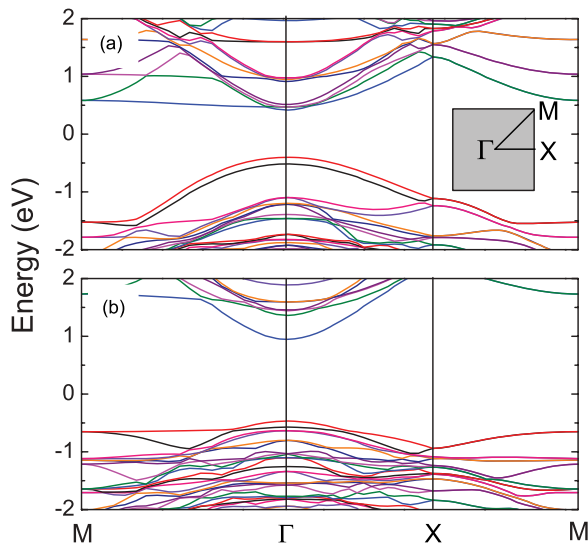
FIG. 3. (Color online) Electronic band structures of the clean (a) TiO_2-terminated and (b) SrO-terminated $SrTiO_3$ (001) surfaces along high-symmetry directions of the surface Brillouin zone (SBZ) shown in the inset.

The surface Brillouin zone (SBZ) of the $\sqrt{2}a \times \sqrt{2}a$ two-dimensional supercell is shown as the inset of panel (a). In the following of the paper, we always use the same SBZ since all structures studied have the same two-dimensional supercell. As can be seen from Fig. 3(a) for the TiO_2-terminated surface, there are two nearly degenerate valence bands separated from the conduction bands by a gap of about 1 eV. These two valence bands are derived from the $2p$ orbitals of O atoms in the surface TiO_2 layers of the two-sided slab. The bottom of the conduction band is contributed by the $3d$ orbitals of Ti atoms in the deep layers. As a contrast, for the SrO-terminated surface in Fig. 3(b), the top valence band is formed by the $2p$ orbitals of O atoms in the deep layers, while the bottom conduction band originates from the $3d$ orbitals of subsurface Ti atoms. The band gaps of the clean $SrTiO_3$ surface are thus determined by the orbitals of O and Ti atoms for both terminations. These results are consistent with the previous calculations.[18,19]

The band structures of an isolated FeSe monolayer with lattice parameter of 3.91 Å in the nonmagnetic and collinear antiferromagnetic states are shown in Figs. 4(a) and 4(b), respectively. As we see, there are two electron-type bands and two hole-type bands around the Γ point in the nonmagnetic state, which is due to the band-folding effect since here the unit cell is $\sqrt{2} \times \sqrt{2}$ unit cell of bulk FeSe on the ab plane.[25] In the collinear antiferromagnetic state,[8] an obvious feature is the Dirac-cone-like band at the Γ point along M-Γ-X with the Fermi level slightly below the Dirac point and the tiny density of states at the Fermi level. The isolated FeSe monolayer in the collinear antiferromagnetic state thus behaves like a slightly doped semiconductor.

B. FeSe on TiO_2-terminated $SrTiO_3$

1. Monolayer FeSe

For the monolayer FeSe on TiO_2-terminated $SrTiO_3$, the substrate is simulated with a six-layer slab as shown in Fig. 1,
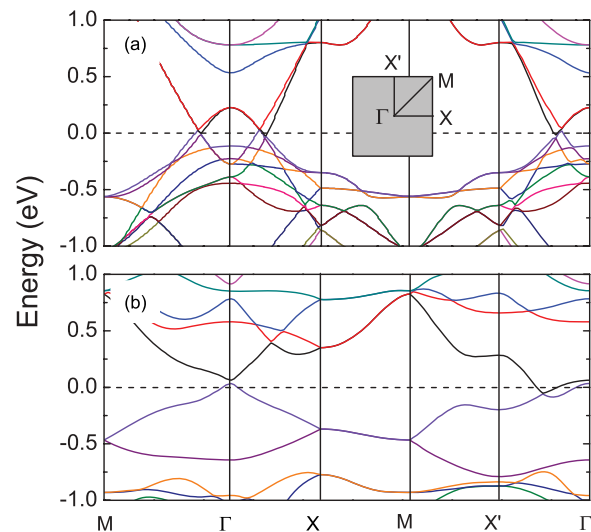
FIG. 4. (Color online) Electronic band structures of an isolated FeSe monolayer along high-symmetry directions of the SBZ: (a) nonmagnetic state; (b) collinear antiferromagnetic state, in which ΓX corresponds to the spins in parallel and $\Gamma X'$ to the spins in antiparallel. The Fermi energy is set to zero.

which eliminates one of the two nearly degenerate top valence bands shown in Fig. 3(a).

The band structures of structures I and II (Fig. 1) for the monolayer FeSe on TiO_2-terminated $SrTiO_3$ in the nonmagnetic state along high-symmetry directions of SBZ are shown in Figs. 5(a) and 5(b), respectively. For both structures, there are two electron-type bands and two hole-type bands around the Γ point, similar to the case of the isolated monolayer FeSe, which is clearly due to the band-folding effect. The main difference of Fig. 5(a) from 5(b) is the relative position of the band at the Γ point just below the Fermi level [blue line in Fig. 5(a) and yellow line in Fig. 5(b)]. This band touches the Fermi level at the Γ point for structure I, while it falls
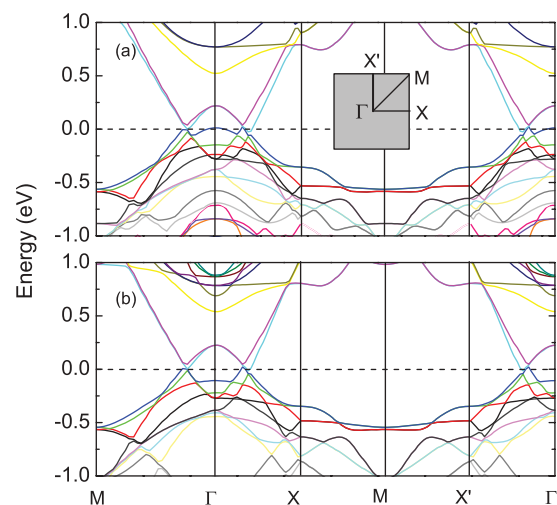
FIG. 5. (Color online) Electronic band structures of (a) structure I and (b) structure II for the monolayer FeSe on TiO_2-terminated $SrTiO_3$ (001) in nonmagnetic state along high-symmetry directions of the SBZ shown in panel (a). The Fermi energy is set to zero.
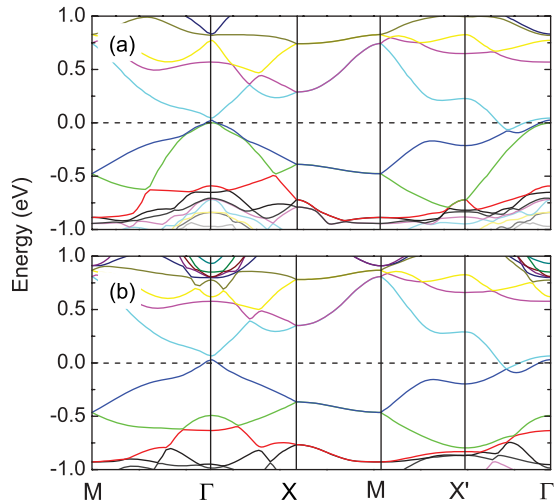
FIG. 6. (Color online) Electronic band structures of (a) structure I and (b) structure II for the monolayer FeSe on TiO_2-terminated $SrTiO_3$ (001) in collinear antiferromagnetic state along high-symmetry directions of the SBZ, in which ΓX corresponds to the spins in parallel and $\Gamma X'$ to the spins in antiparallel. The surface Brillouin zone is shown in the inset of Fig. 5(a). The Fermi energy is set to zero.

FIG. 7. (Color online) Orbital-resolved partial density of states of (a) structure I and (b) structure II for the monolayer FeSe on TiO_2-terminated $SrTiO_3$ (001) in collinear antiferromagnetic state. The Fermi energy is set to zero.

below the Fermi level for structure II, which corresponds to the valence band of the substrate.

By comparing the energies of the nonmagnetic state, ferromagnetic state, checkerboard antiferromagnetic Néel state, and collinear antiferromagnetic state, we find that the ground state is the collinear antiferromagnetic state with a large magnetic moment of 2.5 μ_B on each Fe atom for both structures I and II. In the ground state, the vertical distances of a Se atom to the surface TiO_2 plane are 3.06 and 3.16 Å in structures I and II, respectively. The total energy of structure I is lower by 0.2 eV per surface unit cell than that of structure II. These indicate that the FeSe monolayer has a stronger bonding with the substrate in structure I than in structure II.

Figure 6 shows the band structures of structures I and II for the monolayer FeSe on TiO_2-terminated $SrTiO_3$ in the collinear antiferromagnetic state. Compared with Figs. 3(a) and 4(b), the bands of structure I in Fig. 6(a) look to be a superposition of the bands of the separated substrate and FeSe monolayer. The Fermi level is pinned on the top of the valence band of TiO_2-terminated $SrTiO_3$, i.e., the Dirac-cone-like band of the isolated monolayer FeSe lining up the Fermi level with the parabolic valence band of the substrate. However, such a parabolic band shifts downward away from the Fermi level for structure II in Fig. 6(b).

In order to clarify the contributions to the bands near the Fermi level from different orbitals, we plot the orbital-resolved partial density of states for structures I and II of the monolayer FeSe on TiO_2-terminated $SrTiO_3$ in the collinear antiferromagnetic state in Figs. 7(a) and 7(b), respectively. In both panels, the Fe atom $3d$ orbitals contribute to the density of states around the Fermi level, which is located at a valley. The main difference between Figs. 7(a) and 7(b) is that the $2p$ orbitals of the surface O atoms (red dashed dot-dot line) in TiO_2-terminated $SrTiO_3$ show states near the Fermi level for structure I, while they are absent for structure II. This indicates
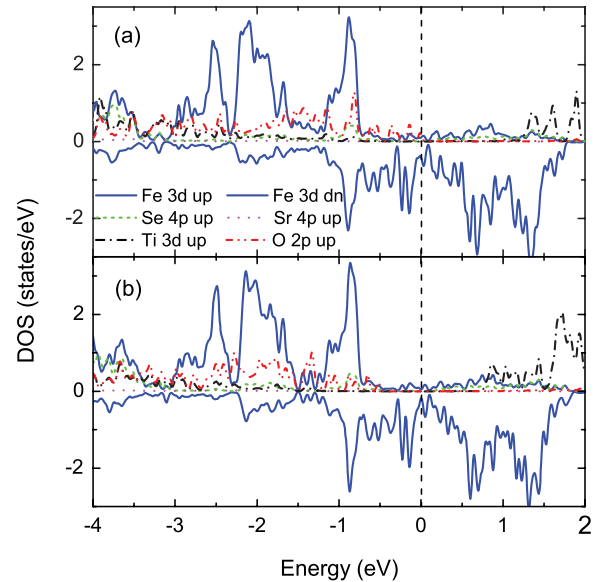
that the parabolic valence band just below the Fermi level in Fig. 6(a) belongs to the surface O atoms, which is further confirmed by the band-decomposed charge density shown in Fig. 8. As can be seen from the side and top views in Fig. 8, this parabolic valence band originates from the p_x and p_y orbitals of the surface O atoms in the TiO_2 termination layer.

2. Bilayer FeSe

For the bilayer FeSe on TiO_2-terminated $SrTiO_3$, the possible positions of first layer of FeSe are structures I and II in Fig. 1, while the second layer of FeSe arranges according to their bulk positions. We still refer them to structures I and II in the following.

Figure 9 shows the band structures of structures I and II for the bilayer FeSe on TiO_2-terminated $SrTiO_3$ in the collinear antiferromagnetic state. Compared with the band
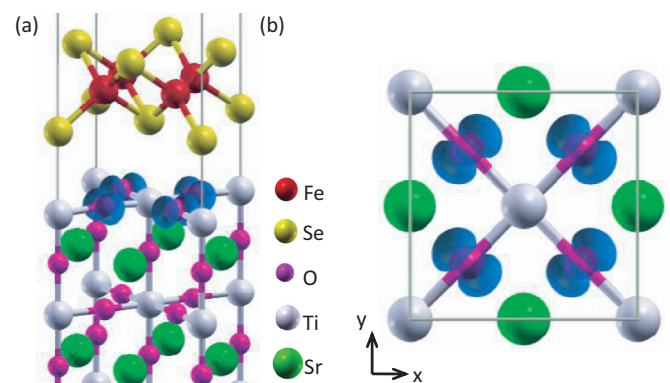
FIG. 8. (Color online) Side view (a) and top view (b) of band-decomposed charge density isosurface (0.001 e/Å^3) of the monolayer FeSe on TiO_2-terminated $SrTiO_3$ (001) in collinear antiferromagnetic state for the parabolic valence band around the Γ point in Fig. 6(a).
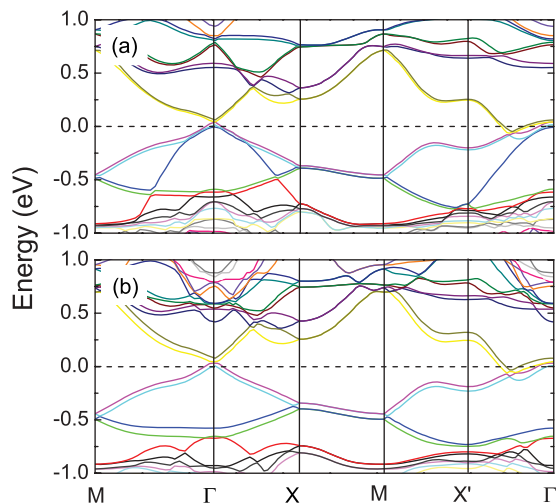
FIG. 9. (Color online) Electronic band structures of (a) structure I and (b) structure II for the bilayer FeSe on TiO_2-terminated $SrTiO_3$ (001) in collinear antiferromagnetic state along high-symmetry directions of the SBZ, in which ΓX corresponds to the spins in parallel and $\Gamma X'$ to the spins in antiparallel. The surface Brillouin zone is shown in the inset of Fig. 5(a). The Fermi energy is set to zero.

structures of the monolayer FeSe on TiO_2-terminated $SrTiO_3$ in Fig. 6, the number of bands near the Fermi level contributed by the Fe atoms is doubled. This feature is similar to the band structure of the bilayer graphene near the K point.[26] Moreover, the parabolic valence band near the Γ point in Fig. 9(a), which originates from the surface O atoms, shows little shift compared with its corresponding band in Fig. 6.

The orbital-resolved partial density of states for structures I and II of the bilayer FeSe on TiO_2-terminated $SrTiO_3$ in the collinear antiferromagnetic state are shown in Figs. 10(a) and
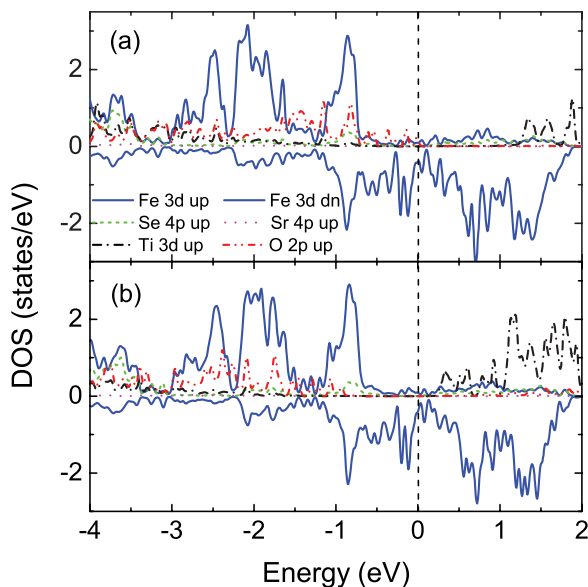
10(b), respectively. Similar to the monolayer case, the Fe atoms contribute to the density of states around the Fermi level, and the surface O atoms of structure I in TiO_2-terminated $SrTiO_3$ show states near the Fermi level, which are due to the parabolic valence band near the Γ point in Fig. 9.

C. FeSe on SrO-terminated $SrTiO_3$

1. Monolayer FeSe

The band structures of structures I and II for the monolayer FeSe on SrO-terminated $SrTiO_3$ in the nonmagnetic state along high-symmetry directions of SBZ are shown in Figs. 11(a) and 11(b), respectively. Referring to Figs. 3(b) and 4(a), for both structures I and II, we see that there are two electron-type bands and two hole-type bands around the Γ point of the SBZ, derived from the FeSe layer. Meanwhile, the parabolic valence bands just below Fermi level come from the valence bands of the substrate. In both cases, the Fermi level is thus pinned onto the top of the valence bands of the substrate.

By comparing the energies of the nonmagnetic state, ferromagnetic state, checkerboard antiferromagnetic Néel state, and collinear antiferromagnetic state, we find that the ground state of the monolayer FeSe on SrO-terminated $SrTiO_3$ is also the collinear antiferromagnetic state with a large magnetic moment, similar to the case of TiO_2 termination. In this state, the vertical distances of a Se atom to the surface SrO plane are 3.67 and 3.64 Å in structures I and II, respectively. The total energy of structure II is slightly lower by 0.06 eV per surface unit cell than that of structure I.

Figure 12 shows the band structures of structures I and II for the monolayer FeSe on SrO-terminated $SrTiO_3$ in the collinear antiferromagnetic state. Likewise, the bands near the Fermi level look like a superposition of the bands of the substrate in Fig. 3(b) and the isolated FeSe monolayer in Fig. 4(b), similar to the case of TiO_2 termination. Likewise, for both structures I and II, the Fermi level is pinned onto the top of the valence

FIG. 10. (Color online) Orbital-resolved partial density of states of (a) structure I and (b) structure II for the bilayer FeSe on TiO_2-terminated $SrTiO_3$ (001) in collinear antiferromagnetic state. The Fermi energy is set to zero.
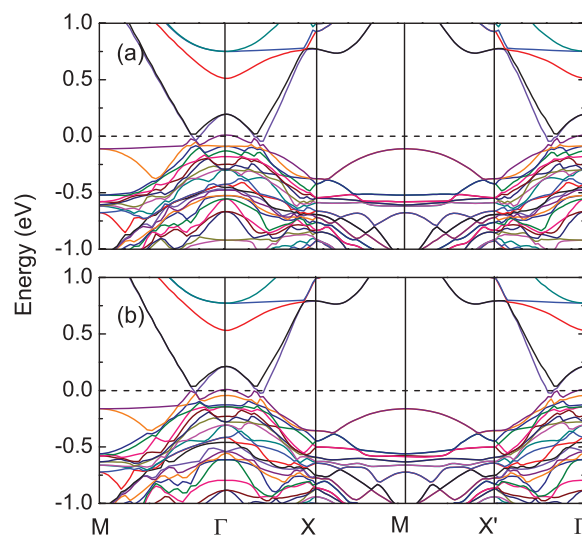
FIG. 11. (Color online) Electronic band structures of (a) structure I and (b) structure II for the monolayer FeSe on SrO-terminated $SrTiO_3$ (001) in nonmagnetic state along high-symmetry directions of the SBZ. The SBZ is shown in the inset of Fig. 5(a). The Fermi energy is set to zero.
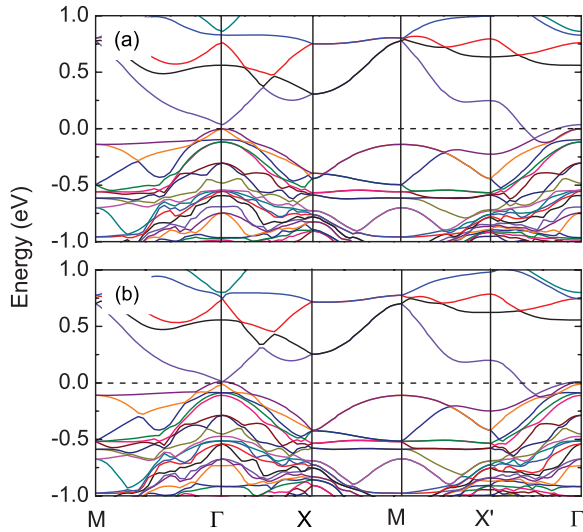
FIG. 12. (Color online) Electronic band structures of (a) structure I and (b) structure II for the monolayer FeSe on SrO-terminated SrTiO$_3$ (001) in collinear antiferromagnetic state along high-symmetry directions of the SBZ, in which ΓX corresponds to the spins in parallel and $\Gamma X'$ to the spins in antiparallel. The surface Brillouin zone is shown in the inset of Fig. 5(a). The Fermi energy is set to zero.

FIG. 13. (Color online) Orbital-resolved partial density of states of (a) structure I and (b) structure II for the monolayer FeSe on SrO-terminated SrTiO$_3$ (001) in collinear antiferromagnetic state. The O-s denotes surface O atom in SrO termination layer and the O-c is O atom in the TiO$_2$ deep layers. The Fermi energy is set to zero.

bands of the substrate after the bands lining up between the monolayer FeSe and the SrO-terminated substrate. However, there is an obvious difference between the bands shown in Figs. 12 and 6. This originates from the different characteristics of SrO- and TiO$_2$-terminated surfaces, for which the Ti-O bond shows considerable covalency near the surface.[18,19]

The orbital-resolved partial density of states for structures I and II of the monolayer FeSe on SrO-terminated SrTiO$_3$ in the collinear antiferromagnetic state are shown in Figs. 13(a) and 13(b), respectively. The O-s denotes surface O atom in the SrO termination layer and the O-c is O atom in the TiO$_2$ deep layers. In both panels, the Fe atoms contribute most to the density of states around the Fermi level, which is located at a valley. However, the O atoms in the TiO$_2$ deep layers contribute more states near the Fermi level than the surface O atoms in the SrO termination. This is consistent with the previous calculations that the upper valence band for the SrO-terminated surface is mainly formed from the orbitals of internal O atoms rather than the surface O atoms.[18,19]

In order to illustrate the origin of the parabolic valence band near Fermi level along the M-Γ-X direction in Fig. 12, the band-decomposed charge density is plotted in Fig. 14. As can be seen from the side and top views, this parabolic band originates from the 2p orbitals of O atoms in the TiO$_2$ deep layers. This is in agreement with the density of states in Fig. 13.

2. Bilayer FeSe

Similar to the case of TiO$_2$ termination, for the bilayer FeSe on SrO-terminated SrTiO$_3$, the possible positions of first layer of FeSe are structures I and II in Figs. 2(a) and 2(b), respectively. The second layer of FeSe arranges according to their bulk positions.

Figure 15 shows the band structures of structures I and II for the bilayer FeSe on SrO-terminated SrTiO$_3$ in the collinear
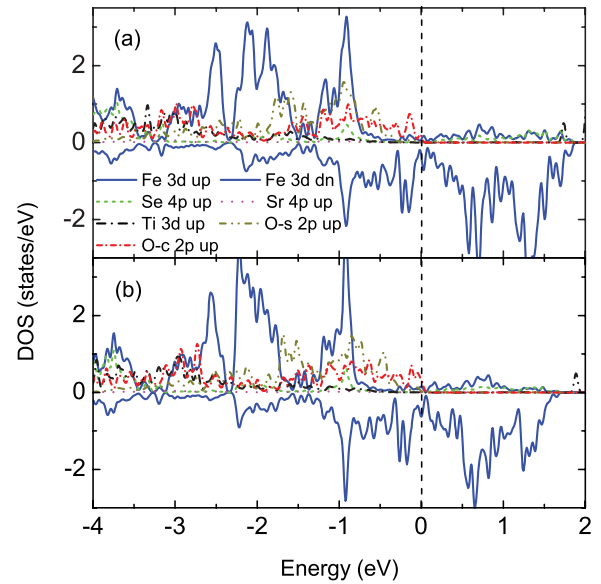
antiferromagnetic state. As can be seen near the Fermi level, the number of bands contributed by the Fe atoms is doubled as well. The parabolic valence band near the Γ point in Fig. 15(a), which originates from O atoms in the TiO$_2$ deep layers, shows slight shift compared with its corresponding band in Fig. 12.

Figure 16 shows the orbital-resolved partial density of states for structures I and II of the bilayer FeSe on SrO-terminated SrTiO$_3$ in the collinear antiferromagnetic state. Similar to the previous results, the Fe atoms contribute to the density of state around the Fermi level responsible for the Dirac-cone-like bands along the M-Γ-X direction in Fig. 15. The 2p orbitals of O atoms in the TiO$_2$ deep layers also show larger density of states near the Fermi level than the surface O atoms. Structures I and II have similar peaks in all energy ranges.
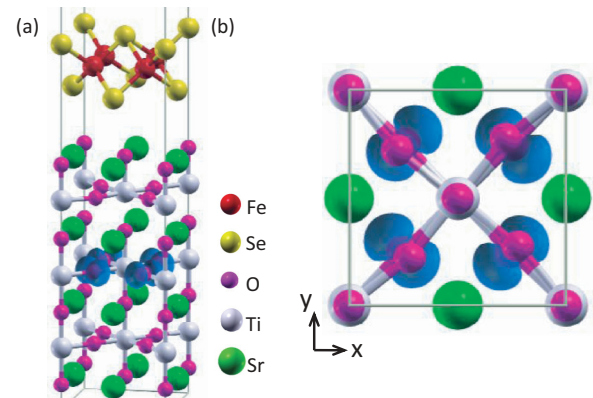
FIG. 14. (Color online) Side view (a) and top view (b) of band-decomposed charge density isosurface (0.001 e/Å^3) of the monolayer FeSe on SrO-terminated SrTiO$_3$ (001) in collinear antiferromagnetic state for the parabolic valence band near the Γ point in Fig. 12.
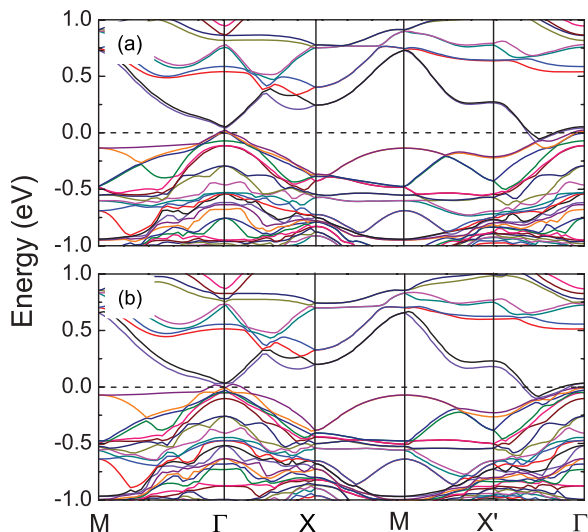
FIG. 15. (Color online) Electronic band structures of (a) structure I and (b) structure II for the bilayer FeSe on SrO-terminated $SrTiO_3$ (001) in collinear antiferromagnetic state along high-symmetry directions of the SBZ, in which ΓX corresponds to the spins in parallel and $\Gamma X'$ to the spins in antiparallel. The surface Brillouin zone is shown in the inset of Fig. 5(a). The Fermi energy is set to zero.

D. FeSe on TiO$_2$-terminated SrTiO$_3$ with electron doping

In the experiment reported in Ref. 14, a superconducting gap was observed by scanning tunneling microscopy in the monolayer FeSe thin film grown on TiO$_2$-terminated SrTiO$_3$. Pristine TiO$_2$-terminated SrTiO$_3$ is an insulator, as shown by the calculated band structure in Fig. 3(a). In the real samples, electrons are usually doped onto the substrate either by introducing O vacancies or doping Nb atoms. To model
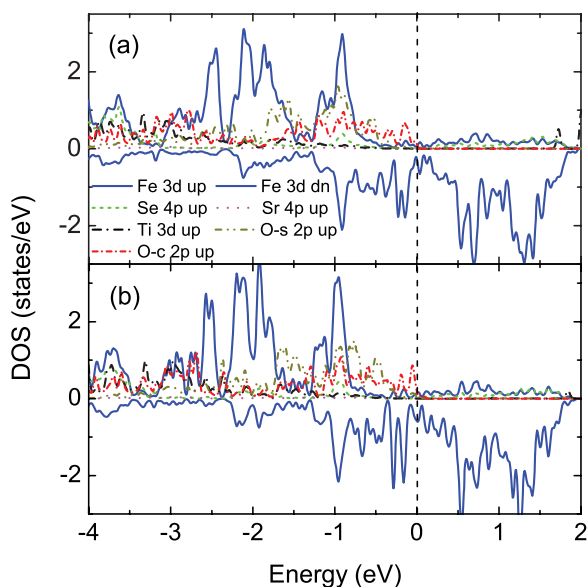
FIG. 16. (Color online) Orbital-resolved partial density of states of (a) structure I and (b) structure II for the monolayer FeSe on SrO-terminated SrTiO$_3$ (001) in collinear antiferromagnetic state. The Fermi energy is set to zero.
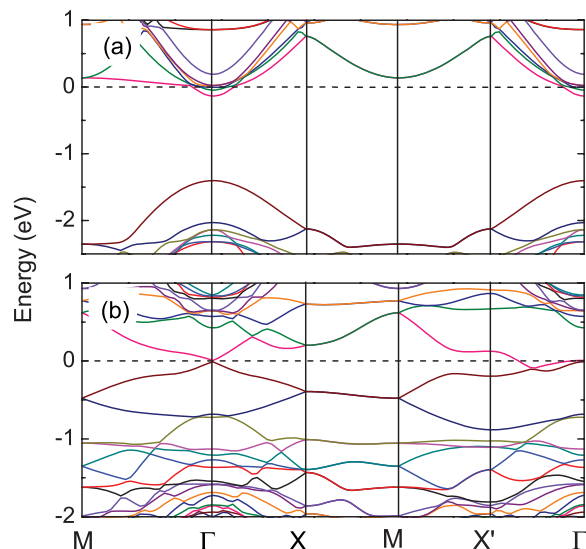
FIG. 17. (Color online) Electronic band structures of (a) TiO$_2$-terminated SrTiO$_{2.97}$F$_{0.03}$ in nonmagnetic state and (b) structure I of the monolayer FeSe on TiO$_2$-terminated SrTiO$_{2.97}$F$_{0.03}$ (001) in collinear antiferromagnetic state along high-symmetry directions of the SBZ, in which ΓX corresponds to the spins in parallel and $\Gamma X'$ to the spins in antiparallel. The surface Brillouin zone is shown in the inset of Fig. 5(a). The Fermi energy is set to zero.

such a doping effect, we have calculated the band structure of the monolayer FeSe on TiO$_2$-terminated SrTiO$_3$ by replacing a small portion of O atoms by F atoms with the conventional virtual-crystal approximation (Refs. 5 and 7). Doping F atoms is not equivalent to introducing oxygen vacancies, but we hope this allows us to gain a qualitative picture on the effect of electron doping in this system.

Figures 17(a) and 17(b) show the band structures of the TiO$_2$-terminated SrTiO$_{2.97}$F$_{0.03}$ with 3% F replacement and the monolayer FeSe on TiO$_2$-terminated SrTiO$_{2.97}$F$_{0.03}$ (structure I) in collinear antiferromagnetic state along high-symmetry directions of the SBZ, respectively. Without the FeSe layer [Fig. 17(a)], such a doping introduces electrons into the conduction band mainly made of Ti 3d orbitals, which eventually pins the Fermi level just above the bottom of the conduction band. This is consistent with the feature of two-dimensional electron gas at the surface of SrTiO$_3$ in angle-resolved photoemission spectroscopy (ARPES) measurements.[27,28] For the monolayer FeSe on TiO$_2$-terminated SrTiO$_{2.97}$F$_{0.03}$ in Fig. 17(b), the Fermi level and the Dirac-cone-like band of FeSe move up together from the top valence band made of O 2p orbitals [in Fig. 6(a)], and finally locates within the band gap of the substrate SrTiO$_{2.97}$F$_{0.03}$. It turns out that the density of states at the Fermi level in a small electron-doping case are reduced since the Fermi level moves away from the top of the valence band. A semiconducting behavior becomes more evident, which is consistent with the experiment.[14] For a heavily doped substrate, for example, 15% F doping, the calculations show that the Fermi level and the Dirac-cone-like bands of FeSe move above into the conduction bands of the substrate.

In addition, in comparison with the case of pristine SrTiO$_3$ substrate in Fig. 6(a), the Fermi level also shows relative shift

with the Dirac point of FeSe, which is more obvious along the X'-Γ direction. In the 3% F replacement, a certain amount of electrons transfer from the substrate into the interface between $SrTiO_{2.97}F_{0.03}$ and the FeSe monolayer. Actually, there is a very small energy gap opening between the upper and lower parts of the Dirac-cone-like band at the Γ point. This small energy gap is found to change with the doping level. In the 3% F doping case, this gap is about 18 meV and the Fermi level locates right within this small energy gap.

IV. DISCUSSION AND SUMMARY

For the undoped $SrTiO_3$ substrate, the most favorable structures for an FeSe monolayer are structure I in Fig. 1(a) on TiO_2-terminated $SrTiO_3$ and structure II in Fig. 2(b) on SrO-terminated $SrTiO_3$. For both structures, the Se atom in the FeSe monolayer is on top of the cation atom of the substrate. Inspection of the orbital- and layer-resolved density of states in the calculations shows that there is no substantial charge transfer between FeSe layers and the undoped $SrTiO_3$ substrate, as expected since both FeSe and $SrTiO_3$ layers are already balanced on the chemical valences. Thus, there is no strong chemical bonding between the FeSe layer and the undoped $SrTiO_3$ substrate. This implies that the electronic band structure of FeSe ultrathin films on $SrTiO_3$ would result from the band lineup at the interface between the FeSe thin film and substrate $SrTiO_3$. The calculations indeed confirm this picture, as shown in Figs. 3, 4, 6, 9, 12, and 15. The Fermi level of FeSe thin films is found to locate at the top of the valence band of substrate $SrTiO_3$. The top valence band of the TiO_2-terminated substrate mainly consists of O-$2p$ orbitals within the TiO_2 surface layer, while O-$2p$ orbitals within deep TiO_2 layers for the SrO-terminated substrate. This band can become conducting by a small amount of hole doping or by applying a small positive gate voltage. In addition, similar to the case of bulk FeSe, the magnetic structures in both FeSe-$SrTiO_3$ heterostructures can be effectively described by a frustrated Heisenberg model with the nearest- and next-nearest-neighbor couplings J_1 and J_2, in which the values of J_1 and J_2 are found to be close to those in the bulk FeSe.[8]

In a recent experiment, the superconductivity in the electron gas formed at the interface between two insulating dielectric perovskite oxides, $LaAlO_3$ and $SrTiO_3$, has been reported.[29] Following ARPES, experiments have found a highly metallic two-dimensional electron gas (2DEG) at the vacuum-cleaved surface of $SrTiO_3$.[27,28] Similar 2DEG has also been observed at the surface of annealed $SrTiO_3$ single crystal by scanning tunneling spectroscopy (STS).[30] Surface oxygen vacancies are believed to introduce such kinds of 2DEG. In the experiment of FeSe-$SrTiO_3$ heterostructure reported in Ref. 14, the superconductivity was found in the FeSe monolayer absorbed onto the TiO_2-terminated substrate, but not in the bilayer films. The Nb-doped (0.5 wt%) $SrTiO_3$ was used in the molecular beam epitaxy (MBE) and low-temperature STS combined system. Both oxygen vacancies and Nb doping in experiments introduce electron doping in $SrTiO_3$. Our F-doping calculations suggest that for lightly electron-doped $SrTiO_3$ (001) with TiO_2 termination, the energy bands of the FeSe monolayer around the Fermi level locate within the energy band gap of the
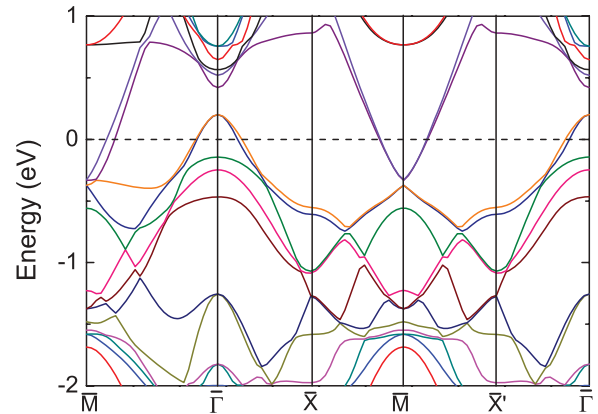
FIG. 18. (Color online) Electronic band structure of structure I for the monolayer FeSe on TiO_2-terminated $SrTiO_{2.97}F_{0.03}$ (001) without structural antiferrodistortion in nonmagnetic state along high-symmetry directions of the SBZ. Here, the surface Brillouin zone is the unfolded one, corresponding to the $a \times a$ unit cell rather than $\sqrt{2}a \times \sqrt{2}a$ supercell. The Fermi energy is set to zero.

substrate (Fig. 17). The conductivity will be thus contributed by the FeSe monolayer alone. In our calculations, the unit cell is doubled due to the structural antiferrodistortion of substrate $SrTiO_3$ in comparison with the case of isolated FeSe layers. The electronic band structures we have shown are all drawn in the folded Brillouin zone, even in the nonmagnetic state. On the other hand, the FeSe ultrathin films on the $SrTiO_3$ substrate without structural antiferrodistortion contain both electron and hole Fermi surfaces in the unfolded zone in the nonmagnetic state, similar to the bulk FeSe material, as shown in Fig. 18. The hole Fermi surfaces are located around the zone center, while the electron Fermi surfaces are located at the zone corner.

We have also studied FeTe ultrathin films on $SrTiO_3$ (001) with TiO_2 termination or SrO termination, and found that the adsorbed FeTe films are also in collinear antiferromagnetic state, different from the bulk FeTe that is in bicollinear antiferromagnetic state.[8] Thus, the superconductivity may likewise happen in the FeTe-$SrTiO_3$ heterostructures, in contrast with the bulk FeTe, in which the superconductivity does not take place.

To summarize, our calculations show that the electronic band structures of the FeSe monolayer and bilayer on TiO_2 termination have similar electronic band structures. Both show a semiconducting behavior. This suggests that the observed superconductivity happens either just in the interface of FeSe-$SrTiO_3$ heterostructures or in the first layer of FeSe, and the superconducting gap could not be observed in the double FeSe thin films by the experimental measurements because the tunneling current was blocked by the second FeSe layer.

---

*zlu@ruc.edu.cn

†txiang@iphy.ac.cn

[1] Y. Kamihara, T. Watanabe, M. Hirano, and H. Hosono, J. Am. Chem. Soc. **130**, 3296 (2008).

[2] M. Rotter, M. Tegel, and D. Johrendt, Phys. Rev. Lett. **101**, 107006 (2008).

[3] X. C. Wang, Q. Q. Liu, Y. X. Lv, W. B. Gao, L. X. Yang, R. C. Yu, F. Y. Li, and C. Q. Jin, Solid State Commun. **148**, 538 (2008).

[4] F.-C. Hsu, J.-Y. Luo, K.-W. Yeh, T.-K. Chen, T.-W. Huang, P. M. Wu, Y.-C. Lee, Y.-L. Huang, Y.-Y. Chu, D.-C. Yan, and M.-K. Wu, Proc. Natl. Acad. Sci. USA **105**, 14262 (2008).

[5] F. Ma and Z.-Y. Lu, Phys. Rev. B **78**, 033111 (2008).

[6] C. de la Cruz, Q. Huang, J. W. Lynn, J. Li, W. Ratcliff II, J. L. Zarestky, H. A. Mook, G. F. Chen, J. L. Luo, N. L. Wang, and P. Dai, Nature (London) **453**, 899 (2008).

[7] F. Ma, Z.-Y. Lu, and T. Xiang, Phys. Rev. B **78**, 224517 (2008).

[8] F. Ma, W. Ji, J. P. Hu, Z.-Y. Lu, and T. Xiang, Phys. Rev. Lett. **102**, 177003 (2009).

[9] W. Bao, Y. Qiu, Q. Huang, M. A. Green, P. Zajdel, M. R. Fitzsimmons, M. Zhernenkov, S. Chang, M. Fang, B. Qian, E. K. Vehstedt, J. Yang, H. M. Pham, L. Spinu, and Z. Q. Mao, Phys. Rev. Lett. **102**, 247001 (2009).

[10] K. Seo, B. A. Bernevig, and J. Hu, Phys. Rev. Lett. **101**, 206404 (2008).

[11] C. H. Lee, A. Iyo, H. Eisaki, H. Kito, M. T. Fernandez-Diaz, T. Ito, K. Kihou, H. Matsuhata, M. Braden, and K. Yamada, J. Phys. Soc. Jpn. **77**, 083704 (2008).

[12] T. M. McQueen, M. Regulacio, A. J. Williams, Q. Huang, J. W. Lynn, Y. S. Hor, D. V. West, M. A. Green, and R. J. Cava, Phys. Rev. B **78**, 024521 (2008).

[13] K. Ueno, S. Nakamura, H. Shimotani, A. Ohtomo, N. Kimura, T. Nojima, H. Aoki, Y. Iwasa, and M. Kawasaki, Nat. Mater. **7**, 855 (2008).

[14] Q.-Y. Wang *et al.*, Chin. Phys. Lett. **29**, 037402 (2012).

[15] H. Unoki and T. Sakudo, J. Phys. Soc. Jpn. **23**, 546 (1967).

[16] W. Jauch and A. Palmer, Phys. Rev. B **60**, 2961 (1999).

[17] N. Bickel, G. Schmidt, K. Heinz, and K. Müller, Phys. Rev. Lett. **62**, 2009 (1989).

[18] E. Heifets, R. I. Eglitis, E. A. Kotomin, J. Maier, and G. Borstel, Phys. Rev. B **64**, 235417 (2001).

[19] E. Heifets, R. I. Eglitis, E. A. Kotomin, J. Maier, and G. Borstel, Surf. Sci. **513**, 211 (2002).

[20] G. Kresse and J. Hafner, Phys. Rev. B **47**, 558 (1993); G. Kresse and J. Furthmüller, Comput. Mater. Sci. **6**, 15 (1996); Phys. Rev. B **54**, 11169 (1996).

[21] P. E. Blöchl, Phys. Rev. B **50**, 17953 (1994); G. Kresse and D. Joubert, *ibid*. **59**, 1758 (1999).

[22] J. P. Perdew, K. Burke, and M. Ernzerhof, Phys. Rev. Lett. **77**, 3865 (1996).

[23] F. El-Mellouhi, E. N. Brothers, M. J. Lucero, and G. E. Scuseria, Phys. Rev. B **84**, 115122 (2011).

[24] J. Neugebauer and M. Scheffler, Phys. Rev. B **46**, 16067 (1992).

[25] A. Subedi, L. J. Zhang, D. J. Singh, and M. H. Du, Phys. Rev. B **78**, 134514 (2008).

[26] T. Ohta, A. Bostwick, T. Seyller, K. Horn, and E. Rotenberg, Science **313**, 951 (2006).

[27] A. F. Santander-Syro, O. Copie, T. Kondo, F. Fortuna, S. Pailhès, R. Weht, X. G. Qiu, F. Bertran, A. Nicolaou, A. Taleb-Ibrahimi, P. Le Fèvre, G. Herranz, M. Bibes, N. Reyren, A. Apertet, P. Lecoeur, A. Barthélémy, and M. J. Rozenberg, Nature (London) **469**, 189 (2011).

[28] W. Meevasana, P. D. C. King, R. H. He, S.-K. Mo, M. Hashimoto, A. Tamai, P. Songsiririthigul, F. Baumberger, and Z.-X. Shen, Nat. Mater. **10**, 114 (2011).

[29] N. Reyren, S. Thiel, A. D. Caviglia, L. Fitting Kourkoutis, G. Hammerl, C. Richter, C. W. Schneider, T. Kopp, A.-S. Rüetschi, D. Jaccard, M. Gabay, D. A. Muller, J.-M. Triscone, and J. Mannhart, Science **317**, 1196 (2007).

[30] R. Di Capua, M. Radovic, G. M. De Luca, I. Maggio-Aprile, F. Miletto Granozio, N. C. Plumb, Z. Ristic, U. Scotti di Uccio, R. Vaglio, and M. Salluzzo, arXiv:1202.0634.

[31] A. Kokalj, Comput. Mater. Sci. **28**, 155 (2003). Code available from [http://www.xcrysden.org].